RSC Advances

ROYAL SOCIETY
OF CHEMISTRY

PAPER

View Article Online
View Journal | View Issue

Check for updates

Cite this: *RSC Adv.*, 2025, **15**, 4014

Injectable carboxymethyl chitosan/oxidized dextran hydrogels containing zoledronic acid modified strontium hydroxyapatite nanoparticles

Alkin Ozgen,[a] Busra Kilic,[b] Mohammadreza Ghaffarlou,[a]
Cagatay Karaaslan[b] and Halil Murat Aydin *[ac]

Nanocomposite hydrogels have potential in bone regeneration due to the inorganic and polymeric material content. In this study, new types of nanocomposite hydrogels composed of zoledronic acid/strontium hydroxyapatite nanoparticles and carboxymethyl chitosan/oxidized dextran (CMC/OD) hydrogels were reported. Pure hydroxyapatite, 5%, 10% and 15% (w/w) strontium-substituted strontium hydroxyapatite nanoparticles were produced and then modified with zoledronic acid at ratios of 5% to 7.5% (w/w). These modified structures were then incorporated into CMC/OD hydrogels. Zoledronic acid modified strontium hydroxyapatite nanoparticles were characterized using Scanning Electron Microscopy (SEM), Energy Dispersive X-ray Spectroscopy (EDS) and X-ray Diffraction (XRD). CMC/OD structures were investigated using Fourier Transform Infrared Analysis (FTIR), Scanning Electron Microscopy (SEM). The physical properties of the hydrogels were determined *via* degradation behavior and rheological measurements. Cell–material interactions were investigated *in vitro*. The results showed that the incorporation of hydroxyapatite nanoparticles into CMC would significantly improve the rheological properties. The addition of strontium to hydroxyapatite nanoparticles significantly enhanced cell proliferation. In addition, a significant increase in alkaline phosphatase (ALP) and calcium deposition was observed with the addition of zoledronic acid. In conclusion, the nanocomposite hydrogels of CMC/OD containing zoledronic acid modified strontium hydroxyapatite demonstrate potential for orthopedic and craniofacial applications due to their superior properties, including the ability to be easily injected into targeted areas, potent antibacterial activity that helps prevent infections and remarkable self-healing capabilities that promote tissue regeneration and repair.

Received 15th November 2024
Accepted 10th January 2025

DOI: 10.1039/d4ra08123d

rsc.li/rsc-advances

1. Introduction

Bone offers a multitude of purposes, including the formation of the main support structure design, being the binding site and mechanical support for muscles and tendons.[1] Bone is not homogeneously solid, it is composed of living bone cells, collagen fibers and inorganic minerals in the form of small crystals in a biomineral environment.[2] Bone defects pose a major surgical challenge and significantly reduce the quality of life of patients due to their limited regenerative potential.[3] Biomaterial-based tissue engineering and regenerative medicine methods have exciting potential to overcome such disadvantages.[4]

The most effective successful osteoinductive materials for the treatment of bone injuries are grafts and calcium phosphate ceramic materials such as hydroxyapatite.[5] However, allografts and xenografts have disadvantages such as high cost, limited availability, the challenge of developing personalized products and risk of disease transmission.[6,7] Calcium phosphates, the primary component of bone, primarily consist of calcium and phosphate, along with trace amounts of magnesium, carbonate, hydroxyl, chloride, and fluoride ions. Due to the natural presence of H_2PO^{4-} and PO_4^{3-} ions in the inorganic phase of bone, calcium phosphate-based graft materials show excellent biological activity in orthopedic applications. Calcium phosphates have a porous structure that allows blood and body fluids to penetrate the bone. This feature increases the material's dissolution rate and enhances tissue–material interaction. The most popular calcium phosphate ceramics are hydroxyapatite (HA) and tricalcium phosphate (TCP). The physical and chemical properties of calcium phosphate ceramics vary depending on the manufacturing processes and conditions. The osteoinductive and osteoconductive properties of calcium phosphate ceramics are important for bone regeneration as they support cell adhesion and proliferation. In particular, properties such as surface roughness, phase content, solubility, crystallinity and porosity affect cell adhesion and proliferation.[8–12] The ability of hydroxyapatite to form tight bonds with native tissues is

---

[a] *Bioengineering Division, Institute of Science, Hacettepe University, Beytepe, Ankara, 06800, Turkey. E-mail: hmaydin@hacettepe.edu.tr*

[b] *Molecular Biology Section, Department of Biology, Faculty of Science, Hacettepe University, Beytepe, Ankara, 06800, Turkey*

[c] *Centre for Bioengineering, Hacettepe University, Beytepe, Ankara, 06800, Turkey*

attributed to its similar structure to minerals found in native bone. Nanoparticle-sized hydroxyapatite has been shown to have improved cytocompatibility.[13–16]

Due to the high flexibility of its structure, HA represents an ideal material to study the chemical, structural, and morphological modifications induced by ionic substitutions. Moreover, enrichment of HA for biomedical applications with biologically relevant ions can improve osteointegration and even provide a tool for local administration of ions with specific therapeutic properties. Among the bivalent cations that can replace calcium in HA, strontium is a trace element present in the human body, notable for its possible biological role.[17] Strontium affects osteoblasts, increasing their proliferation and differentiation.[18] Some studies have reported the effects of strontium-promoted osteogenic differentiation of mesenchymal stem cells, and bone defects were repaired with strontium-containing hydroxyapatite (SrHA) materials.[19–21]

Bisphosphonates represent the major class of drugs used for the treatments of disorders of bone metabolism characterized by increased bone resorption.[22] Bisphosphonates are compounds similar to pyrophosphate that are produced as byproducts in various physiological reactions within human metabolism. The structure of bisphosphonates consists of two phosphate groups linked by phosphoether bonds. The carbon between the phosphate groups makes the structure stable against chemical agents and resistant to enzymes. Therefore, bisphosphonates cannot be converted into metabolites in physiological environments and are excreted unchanged.[23,24] Low bisphosphonate concentrations have a positive effect on osteoblastic function by increasing osteoblast proliferation and differentiation.[25,26] Zoledronic acid, (1-hydroxy-2-imidazol-1-yl-1-phosphonoethyl)phosphonic acid, is a third-generation bisphosphonate with the molecular structure $C_5H_{10}N_2O_7P_2$ and osteoporosis drug approved by the US Food and Drug Administration (FDA) in 2001. Zoledronic acid is included in the aminobisphosphonate group due to nitrogen content and has high affinity with hydroxyapatite. The beneficial effect of zoledronic acid modified hydroxyapatite material on the proliferation and differentiation of osteoblast like MG-63 cells was reported.[27] In the simultaneous presence of zoledronic acid and strontium, strontium is more effective than zoledronic acid on osteoblast proliferation and differentiation. Zoledronic acid has a higher inhibitory effect on osteoclast activity.[28,29]

Recently, injectable biomaterials have been applied in the field of tissue engineering as an alternative to implantation surgery because of their minimally invasive nature.[30] These materials enable surgeons to address bone defects without the need for extensive surgical procedures, thus reducing recovery time and patient discomfort. Injectable hydrogels are especially beneficial due to their ability to conform to irregularly shaped defects in bone. Their gel-like consistency allows for easy application and uniform filling of gaps, ensuring that the material effectively integrates with the surrounding tissue. Additionally, these hydrogels actively promote tissue formation and regeneration by providing a supportive environment for cellular activities. This combination of features makes injectable biomaterials a promising option for enhancing the outcomes of bone healing and restoration.[31] Numerous methods have been used in recent years to make an injectable hydrogel, including redox and photoinitiator-guided polymerization. However, long-term exposure to initiators and irradiation causes cytotoxicity.[32] Therefore, it is important to create a mild environment for the crosslinking of injectable hydrogel networks. The Schiff base reaction is a mild reaction that forms imine bonds through amino groups and aldehyde groups.[33] Natural macromolecules often lack functional groups compared to synthetic macromolecules.[34] However, due to the abundant amino groups in its structure, chitosan is the ideal biomaterial candidate to form an injectable hydrogel based on the Schiff reaction.[35] Chitosan is a deacetylated derivative of chitin and can be modified by carboxymethylation to increase its solubility in common solvents, thereby expanding its range of applications. The addition of carboxymethyl groups to chitosan leads to the formation of anionic derivatives that provide functionality in bioengineering applications.[36] Carboxymethyl chitosan (CMC) is a versatile biopolymer characterized by its water solubility, nontoxic nature, biodegradability, and antibacterial properties. It contains multiple functional chemical groups that effectively promote the adhesion, proliferation, and calcium phosphate deposition of osteoblasts under physiological conditions.[37–39] Due to its excellent biocompatibility, CMC has a wide range of applications in tissue engineering.[36,40] In addition, since it is a hydrophilic, biocompatible, non-toxic, easily processable material, aldehyde modified dextran is frequently used in Schiff base hydrogel studies.[41–44] Dextran is a biocompatible and biodegradable polysaccharide of bacterial origin. The hydroxyl group of dextran could be oxidized to the aldehyde group, which is able to attach to the tissue surface *via* the formation of Schiff base bonds.[45,46] These aldehyde groups enable dextran to function as a macromolecular crosslinker for polymers containing large amounts of amino groups.[47] In addition, dextran also has biofunctions such as hemostasis, wound healing and bacterial growth inhibition.[48] Composite hydrogels have emerged as a promising biomaterial for bone and dental tissue regeneration. Incorporation of hydroxyapatite into composite hydrogels can improve the properties of the biomaterial and allow optimal utilization of hydroxyapatite as part of the scaffold for tissue engineering.[49]

This study reports a new type of carboxymethyl chitosan/oxidized dextran (CMC/OD) hydrogel containing zoledronic acid modified strontium hydroxyapatite nanoparticles. All hydroxyapatite, strontium hydroxyapatite and zoledronic acid containing nanoparticles have been chemically characterized. The synthesized CMC/OD hydrogel structures are morphologically and chemically characterized. Finally, rheological properties and *in vitro* behaviour of the hydrogels containing nanoparticles were studied.

2. Experimental

2.1. Materials

$Ca(NO_3)_2\cdot 4H_2O$ (99%), $Sr(NO_3)_2\cdot 4H_2O$ (99.5%), $Na_3PO_4\cdot 12H_2O$ (≥98%), NaOH (≥97%), zoledronic acid (pharmaceutical secondary standard), chitosan (medium molecular weight), isopropanol (99.5%), ethanol (≥99.5%), hydrochloric acid (37%), calcium acetate (≥99%), hydroxylamine hydrochloride (99%) were provided from Sigma-Aldrich (USA). Chloroacetic acid (99%) was provided from Thermo Scientific Chemicals (USA). Dextran (from *Leuconostoc mesenteroides*, average mol. wt: 35 000–45 000), sodium(*meta*)periodate (≥99%) and ethylene glycol (≥99%) were provided from Sigma-Aldrich (USA). Mouse osteoblastic MC3T3-E1 cell line (CRL-2593) was purchased from the ATCC (Manassas, Virginia, USA). Dulbecco's Modified Eagle Medium (DMEM), MTT and dimethyl sulfoxide (DMSO) solution were obtained from Sigma-Aldrich (USA). Fetal Bovine Serum (FBS), Penicillin/Streptomycin (Pen/Strep) solution and Pierce™ LDH Cytotoxicity Assay Kit were purchased from Thermo Fisher (Massachusetts, USA). The Viability/Cytotoxicity Assay Kit for Animal Live and Dead Cells was provided from Biotium (USA). Alkaline Phosphatase Assay Kit (MAK447) and Calcium Colorimetric Assay Kit (MAK022) were obtained from Sigma-Aldrich (USA). *Escherichia coli* (35218) and *Staphylococcus aureus* (29213) bacterial strains were purchased from the ATCC (Manassas, Virginia, USA). Nutrient broth and bacteriological agar were purchased from Condalab (Madrid, Spain).

2.2. Synthesis of hydroxyapatite (HA) and strontium hydroxyapatite (SrHA) nanoparticles

Hydroxyapatite and strontium hydroxyapatite structures were synthesized using $Ca(NO_3)_2\cdot 4H_2O$, $Sr(NO_3)_2\cdot 4H_2O$ and $Na_3PO_4\cdot 12H_2O$ as starting chemicals. The synthesis was carried out by the precipitation method described previously with minor modifications.[50] In the study, pure hydroxyapatite (HA), hydroxyapatite containing 5% (w/w) strontium (HA5Sr), hydroxyapatite containing 10% (w/w) strontium (HA10Sr) and hydroxyapatite containing 15% (w/w) strontium (HA15Sr) nanoparticles were synthesized. Briefly, calcium nitrate (0.1 M), strontium nitrate (0.1 M), trisodium phosphate solutions (0.1 M) were prepared using deionized water with Ca/P and (Ca + Sr)/P stoichiometric ratios of 1.67. The prepared calcium nitrate and strontium nitrate solutions were added dropwise to the trisodium phosphate solution and the solution was stirred for 2 hours at room temperature. The precipitation conditions of hydroxyapatite and strontium hydroxyapatite crystals were created by bringing the pH value to around 10 with the prepared NaOH. The resulting mixture was filtered under vacuum. The white precipitate was washed with deionized water and dried in the oven at 90 °C for 8 hours. Finally, the powders were calcined at 600 °C for 2 hours.

2.3. Synthesis of zoledronic acid modified hydroxyapatite and strontium hydroxyapatite nanoparticles

At this stage, hydroxyapatite and strontium hydroxyapatite nanoparticles were modified with zoledronic acid at certain ratios. Due to the high solubility of zoledronic acid in NaOH solution, it was selected as drug loading medium. According to hydroxyapatite and strontium hydroxyapatite solid materials, 5% (w/w) and 7.5% (w/w) of zoledronic acid were dissolved separately in NaOH (0.1 M). Then, these solutions and the hydroxyapatite and strontium hydroxyapatite solid materials were taken into separate volumetric flasks and mixed for 12 hours with magnetic stirrer. After mixing, the solutions were centrifuged at 3000 rpm for 3 minutes to precipitate the solid material. Subsequently the solid material was lyophilized.

2.4. Synthesis of injectable carboxymethyl chitosan/oxidized dextran hydrogel

o-Carboxymethyl chitosan (*o*-CMC) was synthesized with slight modifications based on a previously reported study.[51] Medium molecular weight chitosan (5 g) dispersed in isopropanol (50 mL). 50% (w/v) NaOH solution (20 mL) was prepared and added to the mixture. Finally, chloroacetic acid (3 g) was dissolved in isopropanol (10 mL) and added dropwise to the reaction mixture and reacted at 50 °C for 6 hours. After the reaction was terminated with 70% ethanol solution and the CMC sodium salt was filtered. It was washed several times with 70% ethanol (v/v) and was mixed in 37% HCl (10 mL) 70% ethanol (90 mL) solution (v/v) to obtain *o*-CMC. Finally, *o*-CMC was filtered and dried in vacuum. The carboxyl content of *o*-CMC was determined according to the method.[52] *o*-CMC (0.5 g) was dispersed in 2% (w/w) calcium acetate solution (50 mL). The suspension was titrated with 0.1 N NaOH solution using phenolphthalein as indicator. The carboxylic content in the sample was calculated using eqn (1).

$$\text{COOH content (\%)} = \frac{N \times V \times M_w\text{COOH}}{\text{weight of the sample (mg)}} \times 100 \qquad (1)$$

where N is the normality of NaOH, and V is the volume of NaOH in mLs consumed in titration. Oxidized Dextran (O-Dex) was synthesized from the reported work.[53] Dextran (1 g) was dissolved in deionized water (10 mL). Sodium periodate (0.5 g) dissolved in deionized water (5 mL) was added and reacted for 4 hours at room temperature in the dark. The reaction was terminated with ethylene glycol (1 mL). The solution was dialyzed with deionized water in a 12–14 kDa cellulose membrane for 3 days. Finally O-Dex was obtained by lyophilization. The degree of oxidation (aldehyde group content) of O-Dex was determined using the hydroxylamine hydrochloride method.[54] 0.1 g O-Dex was weighed and dissolved in 25 mL of 0.25 N hydroxylamine hydrochloride solution. The mixture was magnetically stirred for 2 hours. Finally, the mixture was titrated with standardised 0.1 N NaOH solution. The number of aldehyde groups per 100 glucose subunits was calculated by the eqn (2):

$$\begin{aligned}\text{CHO content (\%)} &= N \times V \times (\text{MW}_{\text{dex}}/m_{\text{dex}}) \\ &\quad \times (100/S) \times 10^{-3}\end{aligned} \qquad (2)$$

where N is the standardized NaOH concentration, V is the volume of NaOH solution used in the titration, MW_{dex} is the molecular weight of dextran, m_{dex} is the weight of dextran and S is the number of glucose subunits in dextran. Then, polysaccharide-based injectable hydrogels were synthesized based on Schiff base crosslinking. *o*-CMC and O-Dex solutions (2% and 2.5% w/v, respectively) were prepared using PBS (Phosphate Buffered Saline). To prepare composite hydrogels containing nanoparticles, hydroxyapatite nanoparticles were dispersed in O-Dex solution at 1% (w/v). Then the O-Dex solution containing hydroxyapatite was added to the *o*-CMC solution and mixed in a magnetic stirrer. The same procedure was applied for each hydroxyapatite, strontium hydroxyapatite and zoledronic acid modified hydroxyapatite nanoparticles with different contents.

2.5. Characterization of hydroxyapatite (HA) and strontium hydroxyapatite (SrHA) nanoparticles

Scanning Electron Microscopy (SEM) analysis (Gaia 3, Tescan, Czech Republic) was used to study the morphological properties of the synthesized hydroxyapatite and strontium hydroxyapatite nanoparticles. Before analysis, the samples were carbon sputter coated. Energy Dispersive X-ray Spectroscopy (EDS) was used to determine the elemental structure of the samples. The phase analysis of the powder samples was performed with XRD (X-ray Diffraction) (PANalytical Empyrean diffractometer). Within the selected scanning range of $5°(2\theta)$ to $90°(2\theta)$, the intensity data were collected using Cu-Kα radiation ($\lambda = 1.5406$ Å) (voltage = 45 kV and current = 40 mA) with a step scan of $0.1°\ \mathrm{min}^{-1}$. Comparisons with the standard JCPDS (Joint Committee on Powder Diffraction Standards) cards were done to ascertain the phases of the samples.

2.6. Characterization of zoledronic acid modified hydroxyapatite and strontium hydroxyapatite nanoparticles

The elemental content of zoledronic acid modified hydroxyapatite and strontium hydroxyapatite materials were determined by EDS analysis. The effect of zoledronic acid modification on the crystal structure of hydroxyapatite nanoparticles was analyzed by XRD analysis.

2.7. Characterization of CMC/OD hydrogel

2.7.1. Fourier transform infrared spectroscopy (FTIR). FTIR analysis of *o*-CMC and O-Dex structures were performed to prove carboxymethylation in chitosan structure and oxidation in dextran structure. In addition, the functional groups of the synthesized Schiff base hydrogel structure were characterized by FTIR analysis. Attenuated Total Reflection Fourier Transform Infrared spectroscopy (ATR-FTIR, Thermo Fisher, USA) with a resolution of 8 cm^{-1} in the wavelength range of 400–4000 cm^{-1}. On average 16 scans were made for each spectrum.

2.7.2. Scanning electron microscopy (SEM). The morphology of the synthesized CMC/OD hydrogel and CMC/OD hydrogel containing hydroxyapatite nanoparticle was evaluated by Scanning Electron Microscopy (SEM). The samples were freeze-dried for 48 hours and surfaces were coated with carbon 5 nm.

2.7.3. Rheology measurements. The fluid properties of the synthesized hydrogels were evaluated using a Kinexus (Malvern, UK) rheometer. Frequency sweeps were performed at 25 °C, in the frequency range of 0.1–10 hertz and shear stress of 1.5% to determine the elastic modulus (G') and the loss modulus (G'').

2.7.4. Biodegradation analysis. Degradation testing was performed on hydrogel groups with and without hydroxyapatite particles. Samples were lyophilized for 4 week degradation study. The hydrogels were incubated with PBS (10 mL) at 37 °C. PBS was changed daily. The degradation of the hydrogels was calculated as in eqn (3) by evaluating their weight loss after lyophilization.

$$\text{Degradation rate }(\%) = \frac{W_0 - W_\mathrm{r}}{W_0} \times 100 \tag{3}$$

2.8. *In vitro* cytocompatibility analysis

2.8.1. MTT reduction assay. MTT [3-(4,5-dimethylthiazol-2-yl)-2,5-diphenyltetrazolium bromide] assay was performed as previously reported.[55] In 96 well plates, 1×10^4 MC3T3-E1 cells were planted per well. Cells were exposed to various CMC/OD hydrogel extracts for 24 hours. Following incubation, MTT ($0.5\ \mathrm{mg\ mL}^{-1}$) was added to the medium and incubated for 3 hours at 37 °C. To dissolve the formazan crystals, dimethyl sulfoxide solution was added. The intensity of formazan crystals was measured at 570 nm using an EnSight™ Multimode Microplate Reader (PerkinElmer, Massachusetts, USA).

2.8.2. LDH assay. Cells (1×10^4 cells per well) were cultured in 96 well plates and then treated with extracts of CMC/OD hydrogels with different contents for 24 hours. Cytotoxicity was assessed by measuring LDH levels in the supernatants using the Pierce™ LDH Cytotoxicity Assay Kit. The absorbance at 490 nm was read using a microplate reader (PerkinElmer, Massachusetts, USA) with a reference wavelength of 680 nm.

2.8.3. Live/dead cell staining. The Viability/Cytotoxicity Assay Kit for Animal Live and Dead Cells was used to evaluate cell viability and cytotoxicity in accordance with the manufacturer's instructions.[56] Cells were treated with ethidium homodimer-III (4 μM) and calcein-AM (2 μM), and incubated for 30 min at RT. A fluorescence microscope (EVOS FLoid Cell Imaging Station) was then used to evaluate the images.

2.8.4. Alkaline phosphatase (ALP) assay. Alkaline Phosphatase Assay Kit was used to measure ALP activity according to the manufacturer's protocol.[57] Briefly, MC3T3-E1 cells were seeded in novel synthesis gel of different formulation and ALP levels measured for 1, 4 and 7 days. The method utilizes *p*-nitrophenyl phosphate that is hydrolyzed by ALP into a yellow-colored product (maximal absorbance at 405 nm). The rate of the reaction measured spectrophotometrically is directly proportional to the enzyme activity. The cell culture medium was analyzed directly. Each sample (50 μL) was taken into a 96 well plate and working reagent (207 μL) was added using a multi-channel pipettor. The contents of the working reagent were assay buffer (200 μL), magnesium acetate (5 μL) (0.2 M) and *p*NPP liquid (2 μL) (1 M). Purified water (200 μL) (blank well) and calibrator (200 μL) were transferred to separate wells of the 96 well plate. The optical density was read in a plate reader at 405 nm ($t = 0$ min) and again after 4 minutes ($t = 4$ min). All experiments were performed in triplicate.

2.8.5. Calcium deposition assay. Calcium levels were determined using the Calcium Colorimetric Assay Kit according to the manufacturer's instructions.[58] Cells were seeded in novel synthesis gel of different formulation and Ca^{2+} levels measured for 1, 4 and 7 days. Calcium ion concentration is assessed by the chromogenic complex generated between calcium ions and *o*-cresolphthalein. Each sample (50 μL) was taken into a 96 well plate. Chromogenic reagent (90 μL) was added to each well containing standards and samples followed by gently mixing. Then calcium analysis buffer (60 μL) was added to each well and gently mixed. The reaction was incubated at room temperature in the dark for 10 min. Absorbans was then measured at specified wavelengths (575 nm) using EnSight™ Multimode Microplate Reader (PerkinElmer, Massachusetts, USA). All experiments were carried out in triplicate.

2.8.6. Antibacterial activity. The antimicrobial activity of the hydrogels was determined using the agar well diffusion method.[59] G-negative *Escherichia coli* (ATCC 35218) and G-positive *Staphylococcus aureus* (ATCC 29213) were subcultured at 37 °C in nutrient broth medium for 24 hours. After overnight cultures were taken and turbidity corrected to 0.5 McFarland standard, the final inoculum (1.5×10^8 CFU mL^{-1}) was plated onto agar plates. Agar plates were then filled with 100 μL of the produced hydrogel, which served as both a negative/solvent control and a positive control for bacteria (50 μg mL^{-1} of streptomycin and penicillin). Plates were then incubated for 24 hours at 37 °C. The inhibition zone (ZOI) width of the hydrogels was measured and compared to the control groups in order to assess their antibacterial activity. Each measurement was carried out in triplicate.[60]

2.8.7. Statistical analysis. Statistical analysis was performed using Prism 8 (GraphPad Software Inc., California, USA), and a significance level of $p < 0.05$ was applied. A one-way ANOVA with Bonferroni's multiple comparison test was used to compare between the groups. The average of three different biological experiments with SE is what is shown. The following are examples of significant p values: $p < 0.05$ (*); $p < 0.01$ (**); $p < 0.001$ (***); and $p < 0.0001$ (****).

3. Results and discussion

3.1. Characterization of hydroxyapatite (HA) and strontium hydroxyapatite (SrHA) nanoparticles

The scanning electron microscopy (SEM) images of the samples, including hydroxyapatite (HA), HA5Sr, HA10Sr, and HA15Sr, revealed the development of apatite-like structures, as illustrated in Fig. 1. The particle sizes observed across all groups typically ranged from 50 to 130 nanometers, indicating a consistent nano-scale dimension. These nano-sized hydroxyapatite particles exhibit several remarkable properties that distinguish them from their micro-sized counterparts. Notably, they possess enhanced solubility, increased surface area, and superior biocompatibility, making them particularly advantageous for various biomedical applications. The small size of the particles contributes significantly to these properties, enabling improved interactions with biological systems. This characteristic endows nano-sized hydroxyapatite with exceptional bioactivity, making it more advantageous for applications in biomedical fields compared to larger crystalline structures.[61] The morphology of all groups appears to be spherical. Increasing strontium content did not cause any change in the morphological structure of the nanopowders. The strontium concentration for all groups in this study was at a relatively low level, so the risk of disruption of the apatite structure is not high.

Elemental contents and EDS image patterns of pure hydroxyapatite (HA) and hydroxyapatites containing different amounts of strontium (HA5Sr, HA10Sr, HA15Sr) are given in Fig. 2. The EDS elemental map confirmed that calcium was replaced by strontium in different ratios in HA5Sr, HA10Sr and HA15Sr groups. Sr^{2+} (0.12 nm) has a similar ionic radius to Ca^{2+} (0.099 nm) and can replace calcium in the hydroxyapatite structure.[62] A study showed that Sr^{2+} enters the HA lattice and enhances the mechanical strength.[63] Elemental analysis by EDS showed that strontium contents in HA5Sr, HA10Sr and HA15Sr groups were 3.9 ± 0.1%, 7.6 ± 0.1% and 9.5 ± 0.1%, respectively. Stoichiometric (Ca + Sr)/P ratios calculated using atomic percentages are 1.69, 1.62 and 1.48 for HA5Sr, HA10Sr and HA15Sr, respectively. The (Ca + Sr)/P ratio of strontium hydroxyapatite materials synthesized at various ratios was found in the range of 1.5–1.6 and calcium deficiency was explained according to the stoichiometric ratio of 1.67.[64] The stoichiometric (Ca + Sr)/P ratio decreases with increasing strontium content. The stoichiometric Ca/P ratio of mineralized human bone is 1.67.[65] Deviation from the Ca/P ratio of 1.67 weakens the crystal and accelerates the disintegration of the material.[66] Therefore, compared to HA5Sr with a (Ca + Sr)/P ratio of 1.69, HA10Sr with a (Ca + Sr)/P ratio of 1.62 is slightly more bioactive. Similarly, compared to HA10Sr with a (Ca + Sr)/P ratio of 1.62, the calcium-deficient HA15Sr with a (Ca + Sr)/P ratio of 1.48 is slightly more bioactive.

XRD analysis was determined to observe the crystal structure of hydroxyapatite and strontium hydroxyapatite. As shown in Fig. 3B, the major peaks of the synthesized hydroxyapatite match the standard nanohydroxyapatite.[67] It is concluded that all structures were successfully fabricated without any detectable impurity phase. Although decreasing crystal size and crystallinity have been reported with low strontium content, 5%, 10% and 15% strontium content did not cause any significant visible difference in SrHA patterns.[17] However, noisier XRD spectra were obtained with increasing strontium content. Furthermore, as a result of the increase in the amount of strontium, the characteristic peaks of strontium hydroxyapatite are shifted to lower 2θ value. This suggests that strontium hydroxyapatite structures are of lower crystallinity than hydroxyapatite. Increasing strontium content can destabilize the apatite structure and disrupt the crystal symmetry.[68,69] The replacement of strontium with calcium causes a distortion of the phosphate environment. Strontium additions of less than 1.5% did not affect crystallinity, morphology and lattice spacing but slightly increased the crystal size. However, the addition of 15% strontium resulted in lower crystallinity and lattice spacing.[69] This difference was due to the replacement of Ca^{2+} ions with Sr^{2+} ions, which have a larger atomic radius.[70] This indicates that strontium is incorporated into the crystal structure. In addition, it was reported that the hydroxyapatite powders after calcination temperature of 600 °C showed diffraction peaks corresponding to the pure hydroxyapatite phase without any secondary phase. As a result of the

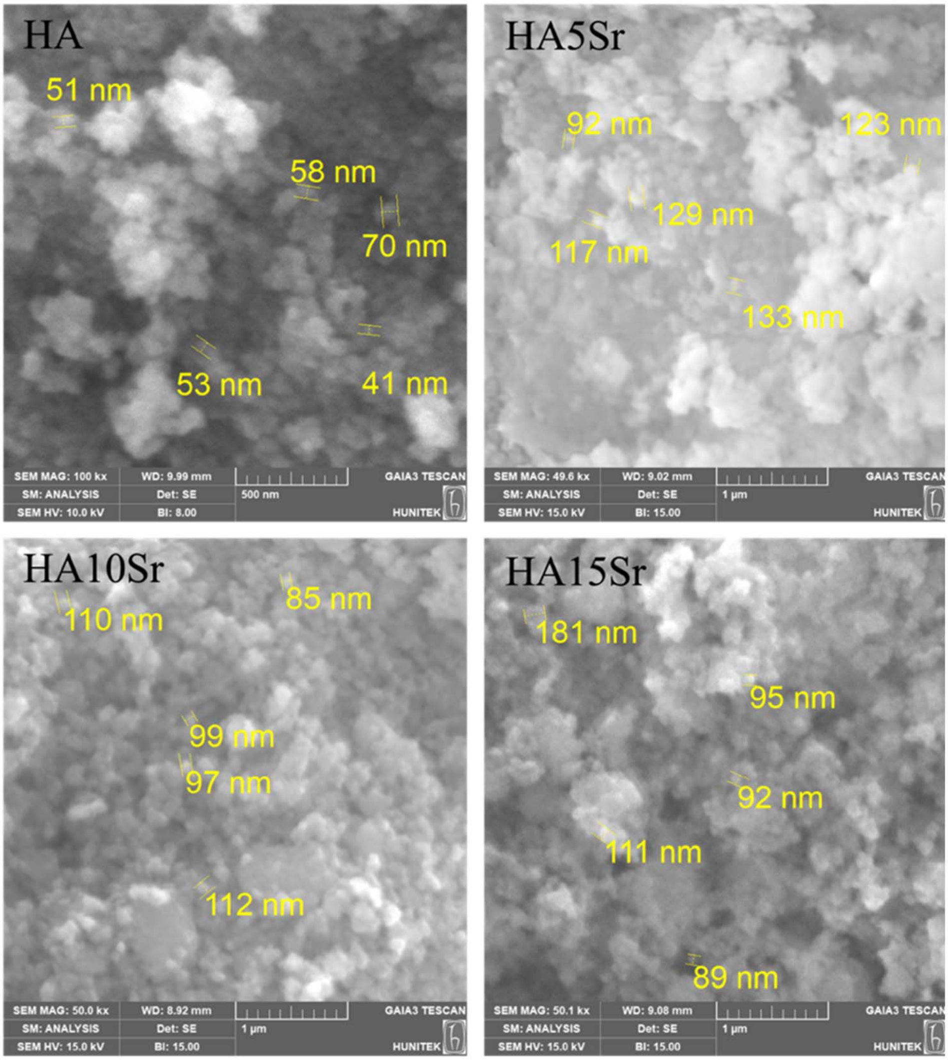

Fig. 1 SEM images of pure hydroxyapatite (HA) and hydroxyapatite containing different amounts of strontium (HA5Sr, HA10Sr, HA15Sr) at 100k×, 49.6k×, 50k× and 50.1k× magnifications, respectively.

calcination temperature, crystallinity increases due to more coalescence of hydroxyapatite crystals.[71]

3.2. Characterization of zoledronic acid modified hydroxyapatite and strontium hydroxyapatite nanoparticles

The elemental content of zoledronic acid modified hydroxyapatite nanoparticles was determined by EDS analysis. The analysis belongs to 7.5% by mass zoledronic acid modified hydroxyapatite sample. According to EDS analysis, the elemental content of the sample is 40.4 ± 0.2% oxygen, 23.7 ± 0.2% carbon, 15.6 ± 0.1% calcium, 14.6 ± 0.1% phosphorus, 3.0 ± 0.4% nitrogen and 2.6 ± 0.0% sodium (Fig. 4). The carbon and nitrogen content in the sample is of zoledronic acid origin. However, the carbon coating process performed before analysis increased the carbon content. Since pure hydroxyapatite does not contain nitrogen, the nitrogen content in the sample is completely attributed to zoledronic acid. In this context, zoledronic acid was proven to be successfully adsorbed on the surface of hydroxyapatite nanoparticles. The high adsorption of zoledronic acid on the hydroxyapatite surface can be attributed to the nitrogen content of zoledronic acid. Nitrogen in the zoledronic acid has the ability to interact with the hydroxyapatite crystal surface.[27] Furthermore, the homogeneous integration of zoledronic acid into the hydroxyapatite structure is evidenced by EDS patterns. The carbon and nitrogen patterns are fully consistent with the calcium, oxygen and phosphorus patterns.

Fig. 5 shows the XRD spectra of hydroxyapatite (HA), zoledronic acid (ZA), zoledronic acid modified HA5ZA and HA7.5ZA formulations. The peaks at 22.8° and 25.6° are clearly characteristic of zoledronic acid.[72] The peaks of zoledronic acid and hydroxyapatite nanoparticles were present in the spectra of HA5ZA and HA7.5ZA formulations. The characteristic zoledronic acid peak around 62° was present in both modified structures. The sharpening of the peak at 40° in the modified structures can be attributed to the presence of zoledronic acid in the structures. Similarly, the peaks observed in the 50–55°

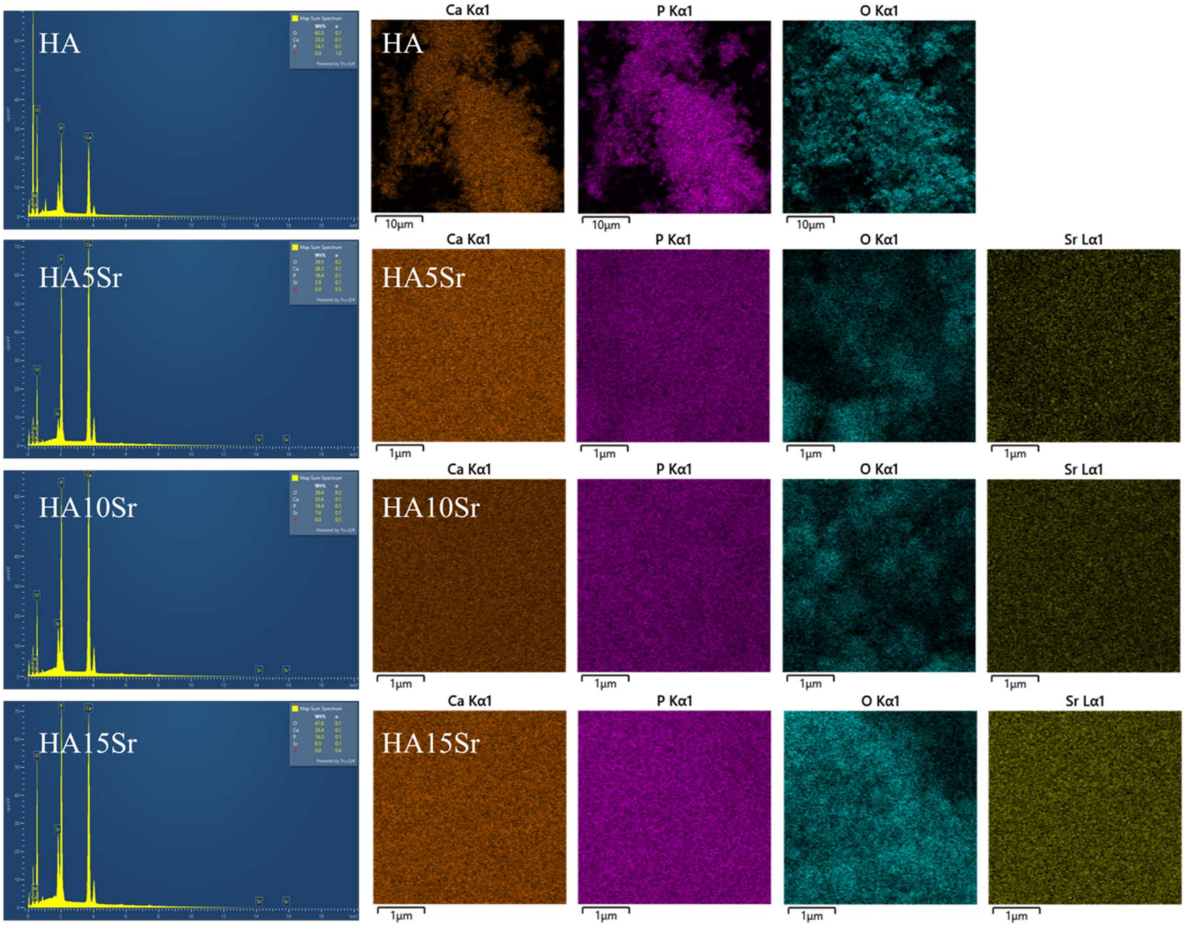

Fig. 2 Elemental contents and EDS image patterns of pure hydroxyapatite (HA) and hydroxyapatite containing different amounts of strontium (HA5Sr, HA10Sr, HA15Sr).

range are of zoledronic acid origin. The low intensity of the peaks is probably due to the low zoledronic acid content in the modified structures.

3.3. Characterization of CMC/OD hydrogel

The preparation of CMC/OD hydrogels was executed without the incorporation of any additional crosslinking agents. The hydrogel formation can be primarily attributed to the Schiff-base reaction, which occurs between the amino groups present in *o*-CMC and the aldehyde groups found in O-Dex. This chemical reaction promotes the interaction between the two biopolymers, leading to the establishment of a stable hydrogel network. The absence of external crosslinking agents not only simplifies the synthesis process but also potentially enhances the biocompatibility and functionality of the resulting hydrogels for various applications.[73] FTIR spectrum of chitosan carboxylation, dextran oxidation and synthesized Schiff base CMC/OD hydrogel are presented in Fig. 6A. Oxidation of dextran resulted in the formation of multiple aldehyde groups along the polymeric chain. The characteristic bond at 1736 cm^{-1} in the O-Dex FTIR spectrum, corresponds to the carbonyl group stretching vibration in the aldehyde structure. This characteristic bond is evidence of O-Dex.[74] The relatively high frequency of the carbonyl group is probably related to the presence of hydrogen bonds in the structure. The main characteristic peaks of chitosan are 3455 cm^{-1} (O–H stretching), 2923–2867 cm^{-1} (C–H stretching) and 1600 cm^{-1} (N–H bending).[75] CMC presents more intensified FTIR adsorption bands in the 1620 cm^{-1} region specific to the –COO– group. This is in agreement with previously published scientific results for CMC.[76] The presence of absorption bands around 3440 cm^{-1}, specific for $-NH_2$ and –OH groups, and a band around 2920 cm^{-1}, specific for $-CH_2$ group, confirms that the basic chemical structure of chitosan is unchanged during synthesis and that the $-NH_2$ group substitution is partial.[77] Before monochloroacetic acid, sodium expanded the hard crystal cross-sections of chitosan, breaking the interaction between the polymer chain layers. As a result, monochloroacetic acid dispersed the chitosan polymer chain more easily.[75] Cross-linking reaction occurred between the amino groups of *o*-CMC and aldehyde groups of O-Dex to form imine bonds. This was confirmed by the appearance of the imine characteristic band at 1628 cm^{-1} in the FTIR spectrum. The decrease in the peak intensity of the aldehyde groups at 1738 cm^{-1} is also evidence of imine bonding.[74] This decrease is due to the reaction of aldehyde groups with amine groups to form imine bonds. The relatively low frequency of the imine

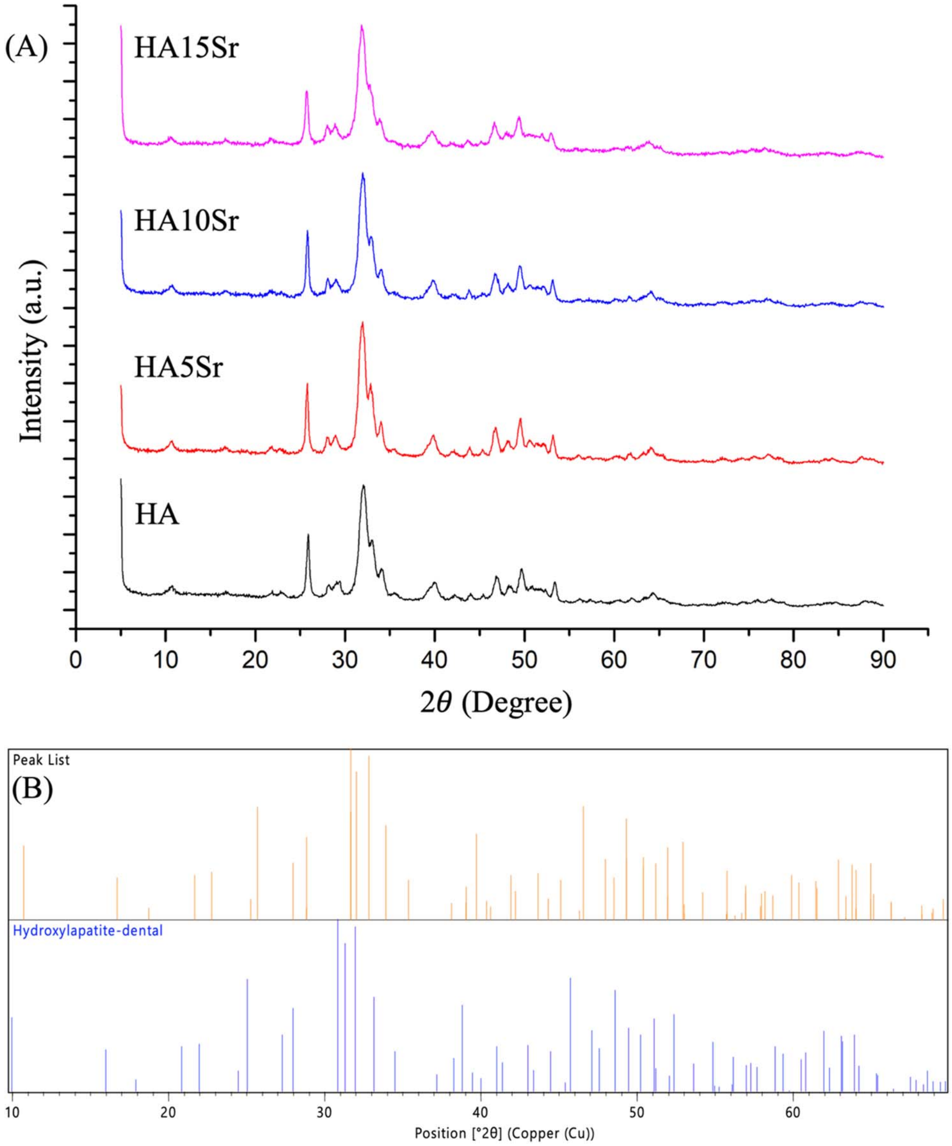

Fig. 3 X-ray powder diffraction (XRD) patterns of hydroxyapatite and strontium hydroxyapatite nanoparticles (A) and standard nano-hydroxyapatite (B).

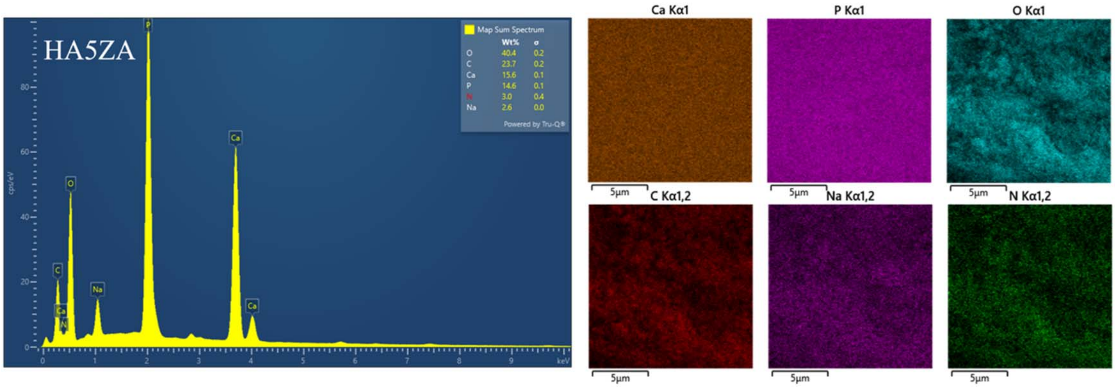

	Wt%	σ
O	40.4	0.2
C	23.7	0.2
Ca	15.6	0.1
P	14.6	0.1
N	3.0	0.4
Na	2.6	0.0

Fig. 4 Elemental content and EDS patterns of pure hydroxyapatite nanoparticles modified with zoledronic acid 7.5% (HA7.5ZA).

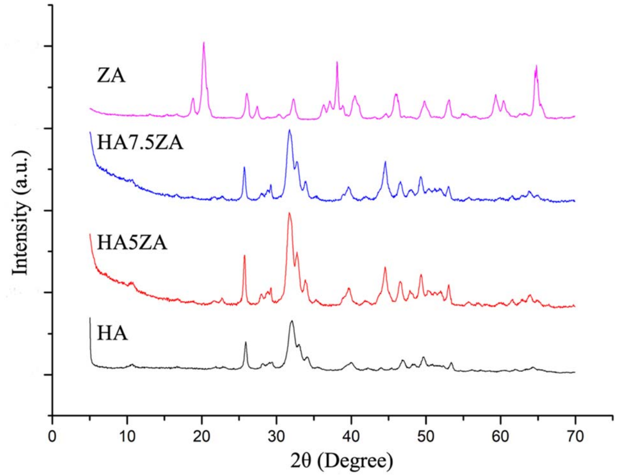

Fig. 5 X-ray powder diffraction (XRD) patterns of pure hydroxyapatite (HA), pure hydroxyapatite nanoparticles modified with zoledronic acid 5% and 7.5% (HA5ZA, HA7.5ZA) and zoledronic acid.

group can be associated with the presence of electron donating groups such as –OH, $-NH_2$ in the structure, steric effects around the amine group and cross-linking. All these possibilities may weaken the imine bond and cause the frequency to shift to a lower value. In addition, the carboxyl content in the synthesised *o*-CMC was calculated as 21.3% and the degree of oxidation in the O-Dex was calculated as 40.5%.

SEM analysis was performed to determine the morphology of freeze-dried hydrogels without particles (Fig. 6B) and hydrogels with particles (Fig. 6C). The presence of particles did not cause any significant change in the hydrogel morphology. Both samples showed a three-dimensional porous structure. This porous structure is due to the ice crystals that are removed from the hydrogel during the lyophilization process. The interconnected micropores present in both structures will provide more space for cell attachment and cell communication.[78] The viscoelastic properties of CMC/OD hydrogel and CMC/OD/HA hydrogel containing hydroxyapatite were evaluated by monitoring the elastic modulus (G') and loss modulus (G'') changes by rheological method. Viscoelastic properties are a critical parameter in determining the mechanical strength of polymeric hydrogels.[79] It was observed that G' values of both samples were higher than G'' from the initial stage (Fig. 6D and E). This is probably due to the rapid gelation processes.[80–82] The high G' value of CMC/OD/HA hydrogel containing hydroxyapatite nanoparticles around 1400 Pa reflects the hardness of the hydrogel. The G' value of CMC/OD hydrogel has lower stiffness due to the absence of hydroxyapatite nanoparticles. Hydrogel scaffold is relatively weak and hence its use is limited to the reconstruction of non-stress bearing bone.[83] In addition, the rheological test results to clarify

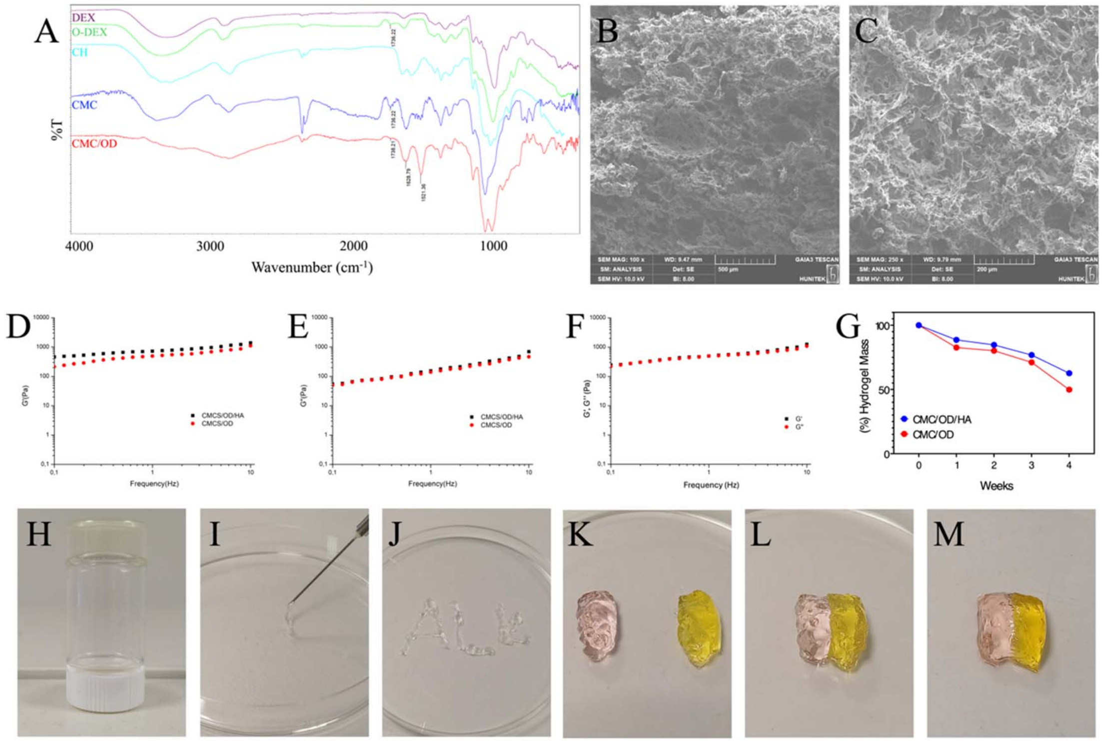

Fig. 6 (A) FTIR spectra of chitosan, CMC, dextran, O-Dex and synthesized CMC/OD hydrogel (B) SEM image of CMC/OD hydrogel at 100× magnifications (C) SEM image of CMC/OD/HA hydrogel containing hydroxyapatite nanoparticles at 250× magnifications (D) comparative rheological graphs of CMC/OD hydrogel and CMC/OD/HA hydrogel for G' (E) comparative rheological graphs of CMC/OD hydrogel and CMC/OD/HA hydrogel for G'' (F) comparative rheological graphs of self-healed CMC/OD hydrogel for G' and G'' (G) degradation rate of CMC/OD control hydrogel and CMC/OD hydrogel (H) CMC/OD hydrogel (I) injectability of CMC/OD/HA hydrogel (J) injectability of CMC/OD/HA hydrogel (K) separate image of colored CMC/OD hydrogels (L) image of reassembled CMC/OD hydrogels (M) image of the reassembled CMC/OD hydrogels after two hours.

the self-healing ability of the hydrogels are shown in Fig. 6F. A decrease in the G' and G'' values of the self-healing CMC/OD hydrogel was observed. However, it is noteworthy that this decrease is <10%. The close elastic modulus values of the original and healed hydrogels indicate that the elastic properties are largely recovered after healing.

Degradation rate of CMC/OD control hydrogel and CMC/OD hydrogel containing hydroxyapatite nanoparticles was studied in PBS solution (0.01 M, pH = 7.4) at 37 °C. As shown in Fig. 6G, the hydrogels showed a very slow degradation profile in the initial phase. The weight loss was due to the hydrolysis of imine bonds within the hydrogel networks in PBS. Approximately 15% mass loss was observed after two weeks. The low degradation is due to the fact that the strongly cross-linked CMC and O-Dex chains do not dissolve easily. In the following weeks the hydrogels showed a relatively rapid degradation profile. The rapid degradation profile may be due to the gradual hydrolysis of Schiff-base bonds between CMC and O-Dex chains.[84] The cleavage of imine linkages promoted the bulk-degradation of the hydrogel, and a more loosely network structure in turn led to a faster degradation of the hydrogel.[78] The lower degradation profile of CMC/OD/HA hydrogel containing hydroxyapatite nanoparticles is probably due to the higher crosslink content of the nanohybrid hydrogel.[85] The incorporation of hydroxyapatite into the gelling system significantly enhances the stability of hydrogel scaffolds. Specifically, the use of nanohydroxyapatite increases the crosslinking density within the hydrogel matrix. This heightened crosslinking density has a profound impact on several macroscopic properties of the hydrogels. Additionally, the presence of nanohydroxyapatite results in a slower rate of mass loss over time, providing improved durability. Moreover, these modifications enhance the mechanical properties of the hydrogels, allowing them to better withstand applied stresses and strains. Overall, the integration of hydroxyapatite plays a crucial role in optimizing the performance and longevity of hydrogel scaffolds for various applications.[78]

The Schiff base reaction resulted in the formation of a chemically cross-linked network and a transparent hydrogel. The image of the formed hydrogel is given in Fig. 6H. As seen in Fig. 6I, the hydrogel containing hydroxyapatite nanoparticles was in injectable form. The hydrogel containing nanoparticles was easily injected from the syringe (Fig. 6J). In addition, the self-healing property of the hydrogels was investigated. The colored CMC/OD hydrogels were cut into two halves (Fig. 6K) and then the two halves were brought into contact (Fig. 6L). After two hours at room temperature, the hydrogel self-healed (Fig. 6M). After the healing, no obvious vestige of the physical damage was observed at the junction. The self-healing mechanism is based on the dynamic bonding of the Schiff base between the unreacted aldehyde groups of O-Dex and the amino groups of CMC.[86]

3.4. *In vitro* cytocompatibility and osteogenic induction of the drug-loaded hydrogel

The impact of different formulation of strontium and zoledronic acid loaded CMC/OD hydrogels on mouse embryonic osteoblast precursor (MC3T3-E1) viability and cytotoxicity was examined by MTT and LDH assay (Fig. 7).

It was observed that hydrogel groups showed over 80% viability (Fig. 7A). As the inorganic phase of bone, hydroxyapatite is expected to show high viability and low toxicity. It has been reported that the addition of increasing amounts of strontium does not cause any toxicity in the hydroxyapatite structure, while the addition of low levels of strontium increases cell viability.[87,88] The findings are in line with previous research, given that hydroxyapatite groups that include 5% strontium exhibit greater vitality and reduced toxicity compared to pure hydroxyapatite groups.[89] In addition, it has been explained that low amounts of zoledronic acid content in the hydroxyapatite structure does not cause toxicity.[27,90] Consistent with previous studies, the zoledronic acid containing groups exhibited high cell viability. According to LDH results, necrotic effect was seen

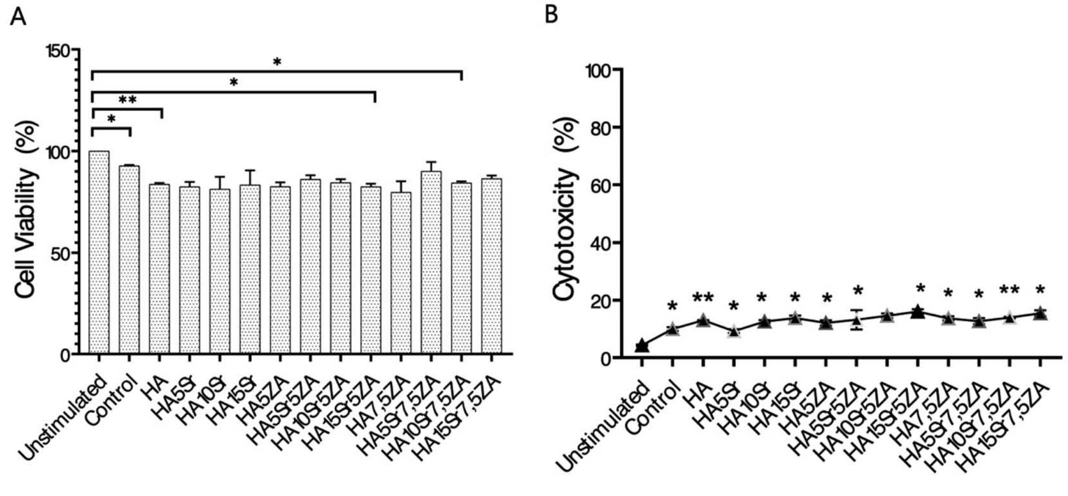

Fig. 7 MTT (A) and LDH (B) results in cells following 24 hours of stimulated with extracts from CMC/HA hydrogels. One-way ANOVA was performed to compare multiple groups and Bonferroni *post hoc* test was applied. *n*: 3, $p > 0.05$ (ns), $*p < 0.05$; $**p < 0.01$; $***p < 0.001$; $****p < 0.0001$. Control: CMC/OD hydrogel without hydroxyapatite nanoparticles.

in below 16% was detected in all hydrogel groups (Fig. 7B). Non-cytotoxic biomaterials have cell viability of over 70%.[91,92] These results confirm the hydrogels non-cytotoxic nature according to ISO 10993-5. The slight necrotic effect can be attributed to the tendency of CMC structure to create an acidic environment. Carboxymethyl groups in CMC structure are acidic groups that can give proton. Acidic conditions can lead to the generation of reactive oxygen species in cells, which decreases cell viability.[93,94] The findings demonstrate that the simultaneous presence of strontium and zoledronic acid has no adverse impact on cell viability. Considering the cell viability and cytotoxicity experiments, strontium and zoledronic acid hydrogels with 5% strontium performed optimally. Based on these results, futher experiments were continued with HA, HA5Sr, HA5Sr5ZA and HA5Sr7.5ZA groups.

The cytocompatibility and osteogenic induction of cells on drug-loaded hydrogels was examined using EtBr/calcein AM fluorescence for 1, 4, 7 days (Fig. 8). The findings showed that osteoblast cells in all groups demonstrate green fluorescence, suggesting that almost all living cells were stained with the calcein AM dye (Fig. 8A). As exhibited in Fig. 8A, osteoblast cells on the various drug-loaded groups proliferated gradually without a significant difference at days 1, 4, and 7, showing that the strontium and zoledronic acid-loaded hydrogel had good biocompatibility. In addition, spindle-like structures were observed, especially in the groups containing strontium and zoledronic acid. The minimal release of strontium and zoledronic acid from certain drug-loaded hydrogel groups highly porous and large surface area may explain their limited cell growth. The limited cell survival of CMC/OD hydrogel groups with high porosity and surface area may be due to restricted strontium and zoledronic acid release. Intracellular calcium deposition is an important feature of osteogenic differentiation, as shown by Fig. 8B. The cells on hydrogel with strontium and zoledronic acid (HA5Sr5ZA) showed considerably higher calcium deposition than the control group after 1 day ($p < 0.001$). The HA5Sr7.5ZA hydrogel exhibited a considerably higher level of calcium deposition than the control group after 4 and 7 days ($p < 0.01$ and $p < 0.05$ respectively). HA5Sr, which includes strontium, showed a statistically significant increase in calcium mineralization after 7 days of culture when compared to the control group ($p < 0.001$). There may be a correlation between calcium deposition and the proliferation of cells. The findings suggest that the substitution of 5% to 10% strontium into the hydroxyapatite ceramic structure may enhance cell proliferation and mineralization.[95,96] Furthermore, zoledronic acid presence was shown to increase osteoblast proliferation in comparison to pure hydroxyapatite align with previous studies.[27] The porous structure of CMC/OD hydrogel has enabled increased interaction of cells with the environment. This porous structure can mimic the natural load-bearing and flexibility properties of bone tissue by becoming more durable and flexible with the integration of hydroxyapatite particles into the structure. The results are consistent with calcium deposition and ALP activity. The upregulation of ALP activity is an essential step in the early stage of osteogenic

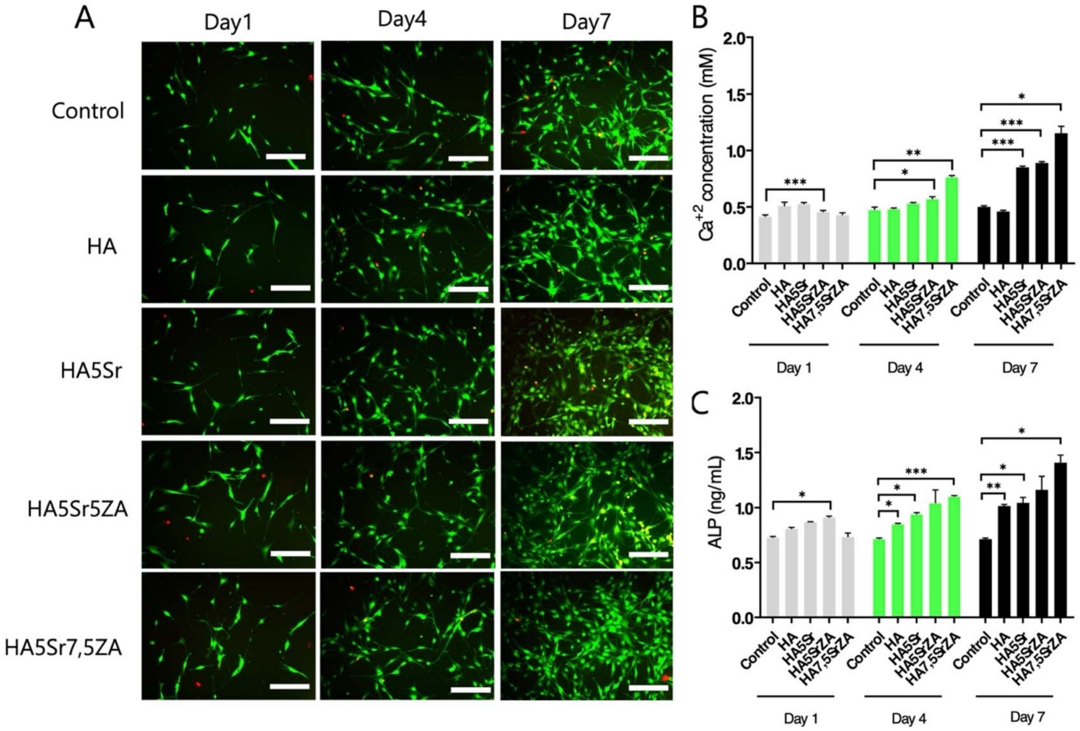

Fig. 8 EtBr/calcein AM fluorescence (A), calcium accumulation (B), and ALP activity (C) in cells on various formulations of strontium and zoledronic acid-loaded CMC/OD hydrogels for 1, 4, and 7 days. One-way ANOVA was performed to compare multiple groups and Bonferroni *post hoc* test was applied. *n*: 3, $p > 0.05$ (ns), $^{*}p < 0.05$; $^{**}p < 0.01$; $^{***}p < 0.001$; $^{****}p < 0.0001$. The scale bar in the fluorescent images represents 125 μm. Control: CMC/OD hydrogel without hydroxyapatite nanoparticles.

differentiation.[97] As shown in Fig. 8C, ALP activity detection indicated that the ALP activity in the HA5Sr5ZA and HA5Sr7.5ZA groups was significantly higher than that in the control, HA, and HA5Sr groups. ALP activity of the hydrogel containing strontium and zoledronic acid (HA5Sr5ZA) was significantly higher than that of the control group ($p < 0.05$) for 1 day. After four days of culture, HA5Sr and HA5Sr7.5ZA hydrogels showed significantly higher ALP activation compared to the control group (respectively $p < 0.05$, $p < 0.001$). There was a notable difference between the control group, HA5Sr and HA5Sr7.5ZA after 7 days. The ALP activation level was highest in the HA5Sr7.5ZA sample compared to the other groups. The sample containing strontium and zoledronic acid had significantly higher ALP activity compared to the control group ($p < 0.05$). A significant increase in ALP activity in the presence of zoledronic acid was noted on day 7 of culture.[27] Both strontium and zoledronic acid have been reported to influence osteoblast proliferation, viability and differentiation.[27,96,98–100] The effects of zoledronic acid on osteoblasts are particularly dose-dependent.[101] At low concentration and in combination with strontium, zoledronic acid showed no cytotoxicity. In addition, it shows a remarkable positive effect on extracellular matrix deposition. The results of the present study are consistent with those previously reported in terms of osteoblast response.[27,28,102]

3.5. Synergistic antimicrobial properties of drug-loaded hydrogels

Bacterial infection delays tissue regeneration and greatly affects wound healing. Therefore, the development of hydrogels with antibacterial properties is great significance in clinical application.[103,104] Therefore, different CMC/OD hydrogels were tested to evaluate their antibacterial activities against G-negative *E. coli* and G-positive *S. aureus*. The area of the inhibition zone of the hydrogels on the plates was directly compared with the control antibiotic (50 μg mL^{-1}) and it was clearly seen that CMC/OD hydrogels inhibited the growth of both *E. coli* and *S. aureus*.

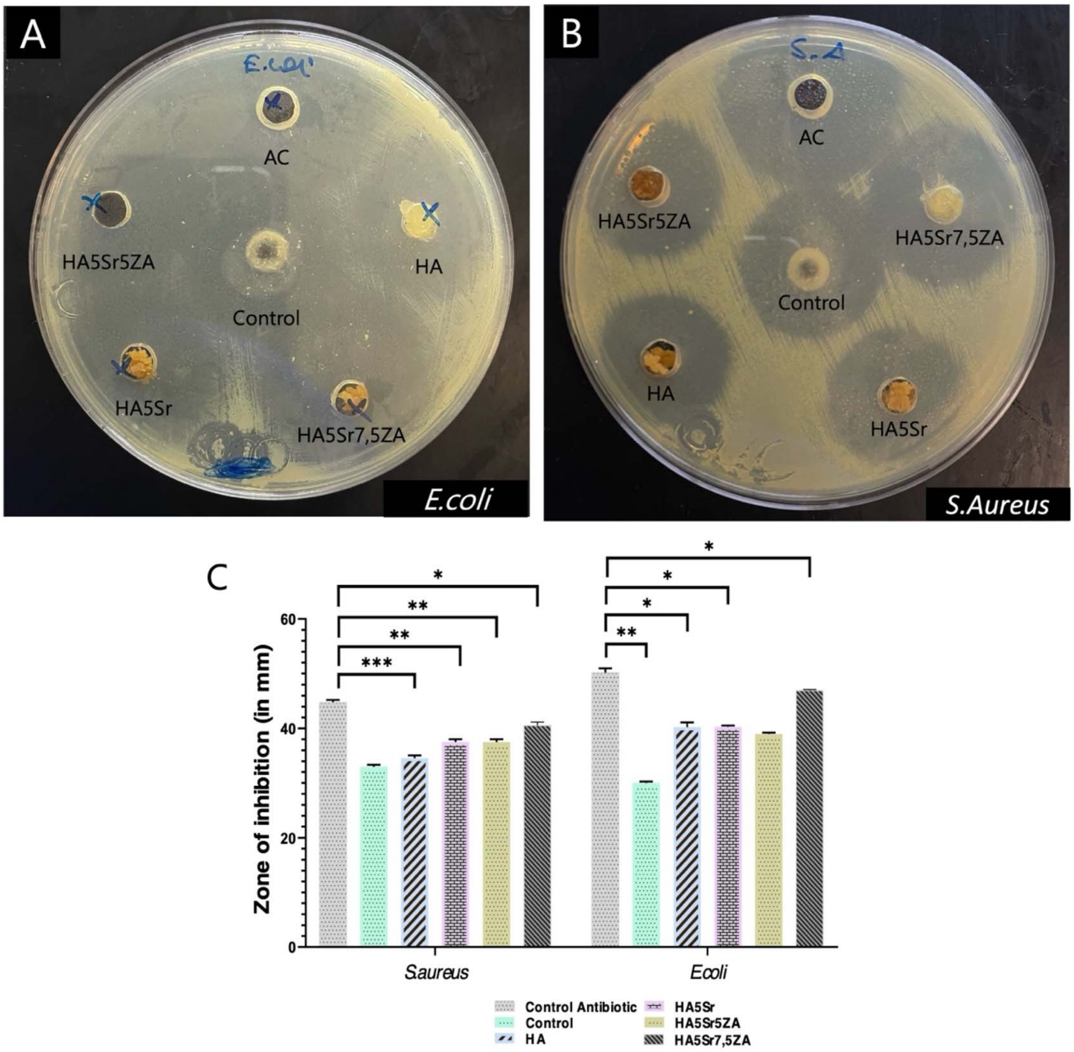

Fig. 9 Antibacterial activity of the various formulations of strontium and zoledronic acid-loaded CMC/OD hydrogels against, *E. coli* (A) and *S. aureus* (B) and Zone inhibition of different hydrogel formulations (C). One-way ANOVA was performed to compare multiple groups and Bonferroni *post hoc* test was applied. *n*: 3, $p > 0.05$ (ns), *$p < 0.05$; **$p < 0.01$; ***$p < 0.001$; ****$p < 0.0001$. Control: CMC/OD hydrogel without hydroxyapatite nanoparticles.

According to the results of the agar disk diffusion test, the hydrogels had an inhibitory effect on the diffusion growth of *E. coli* and *S. aureus* (Fig. 9). In addition, it was concluded that the hydrogels had a more significant inhibitory effect on *E. coli*. CMC/OD (control) group also showed antibacterial activity. Therefore, it is thought that the antibacterial activity is mainly caused by CMC and O-Dex. The amino group of chitosan has developed a mechanism of antibacterial activity by binding to the surface components of bacteria and inhibiting their growth. At lower concentrations, chitosan may bind to the negatively charged bacterial surface and disrupt the cell membrane, leading to cell death. At high concentrations, chitosan is thought to coat the bacterial surface and prevent mass transfer across the cell barrier.[105] The antibacterial activity of chitosan depended on the $-NH_2$ concentration of the polymer and increased with the addition of $-NH_2$ content. In solution, chitosan is a polycationic compound due to the large number of $-NH_3$, so the antibacterial activities of chitosan and carboxymethylated derivatives also depend on the effective number of $-NH_3$ groups.[106]

There is equal $-NH_2$ in the structure of *o*-CMC and chitosan. However, the –COOH group in the *o*-CMC structure may have reacted intermolecularly with $-NH_2$ and loaded amine groups. Under the same condition, *o*-CMC has more $-NH_3$ groups than chitosan. Therefore, the antibacterial activity of *o*-CMC increases.[106] The antibacterial properties of chitosan and *o*-CMC nanoparticles against G-positive *S. aureus* were experimentally demonstrated. Similarly, the antibacterial activity of *o*-CMC nanoparticles is higher than chitosan nanoparticles.[107] The antibacterial activity of O-Dex is probably due to the reaction of aldehyde groups with amino groups in proteins found in cell membranes.[108] The inhibitory activity of O-Dex is explained by the visible effect on the bacterial cell wall and the loss of cytoplasmic contents. In addition, O-Dex has been demonstrated to inhibit motility and chemotaxis.[109] It has been reported that strontium substitution may enhance antibacterial activity against *E. coli* and *S. aureus*. Bacterial activities such as growth and reproduction, cell wall synthesis, cell metabolism and chromosomal replication can be inhibited by the release of Sr^{2+} ions.[110,111] Furthermore, some bisphosphonates have been reported to be effective against bacteria.[112] In addition, higher antibacterial activity against *E. coli* and *S. aureus* has been reported in chitosan nanohydroxyapatite scaffolds containing zoledronic acid compared to chitosan nanohydroxyapatite scaffolds.[113] In conclusion the high antibacterial effect of all groups can be attributed to the combined use of antibacterial agents such as chitosan, dextran and strontium.

4. Conclusion

In the present study, hydroxyapatite nanoparticles with different strontium and zoledronic acid dope grades were synthesized and then incorporated into CMC/OD networks to form a hydrogel structure. The study represents a novel and original report on the reconstruction of bone defects using nHA/Sr/ZA/CMC/OD structures. The hydrogel showed injectability, self-healing, antibacterial properties, porous structure and favorable degradation rate. The CMC/OD hydrogel containing HA5Sr nanoparticles has an optimal concentration of released Sr^{2+} for osteoblast proliferation *in vitro*. Moreover, the hydrogel with low zoledronic acid content showed high activity in terms of ALP and calcium deposition. In conclusion, the composite material CMC/OD, which contains a zoledronic acid modified form of strontium hydroxyapatite, shows significant potential for various applications in the fields of orthopedic and craniofacial surgery. This innovative material boasts exceptional properties that enhance its effectiveness, notably its injectability, which allows for minimally invasive procedures and precise delivery to targeted sites. Additionally, the antibacterial activity of this composite is crucial for reducing the risk of infections, a common concern in surgical interventions. Furthermore, its self-healing capabilities contribute to improved long-term stability and functionality, making it an attractive option for tissue engineering and regenerative medicine. These characteristics position CMC/OD based nanocomposite hydrogels as a promising candidate for advancing treatment methodologies in multiple medical disciplines.

Conflicts of interest

The authors declare no conflict of interest.

Acknowledgements

This study was financially supported by Hacettepe University Scientific Research Projects Coordination Department under the grant number of FHD-20500. Additionally, the authors would like to acknowledge the support provided by Turkish Scientific and Research Council (TÜBİTAK) 1004 – Center of Excellence Support Prog. – High Technology Platforms in Priority Fields (Project number: 22AG004, Next Generation Biomaterial Technologies Research Network for Healthy Life).

References

1 J. Pajarinen, T. Lin, E. Gibon, Y. Kohno, M. Maruyama, K. Nathan, L. Lu, Z. Yao and S. B. Goodman, *Biomaterials*, 2019, **196**, 80–89.
2 V. Uskoković, I. Janković-Častvan and V. M. Wu, *ACS Biomater. Sci. Eng.*, 2019, **5**, 3483–3498.
3 P. Wang, X. Liu, L. Zhao, M. D. Weir, J. Sun, W. Chen, Y. Man and H. H. Xu, *Acta Biomater.*, 2015, **18**, 236–248.
4 S. Saravanan, S. Vimalraj, P. Thanikaivelan, S. Banudevi and G. Manivasagam, *Int. J. Biol. Macromol.*, 2019, **121**, 38–54.
5 A. Asti and L. Gioglio, *Int. J. Artif. Organs*, 2014, **37**, 187–205.
6 H. F. Pereira, I. F. Cengiz, F. S. Silva, R. L. Reis and J. M. Oliveira, *J. Mater. Sci.: Mater. Med.*, 2020, **31**, 1–16.
7 A. Oryan, S. Alidadi, A. Moshiri and N. Maffulli, *J. Orthop. Surg. Res.*, 2014, **9**, 1–27.
8 N. W. Kucko, R.-P. Herber, S. C. Leeuwenburgh and J. A. Jansen, in *Principles of Regenerative Medicine*, Elsevier, 2019, pp. 591–611.
9 J. Jeong, J. H. Kim, J. H. Shim, N. S. Hwang and C. Y. Heo, *Biomater. Res.*, 2019, **23**, 4.
10 M. Navarro, A. Michiardi, O. Castano and J. Planell, *J. R. Soc. Interface*, 2008, **5**, 1137–1158.

11 T. Albrektsson and C. Johansson, *Eur. Spine J.*, 2001, **10**, S96–S101.
12 S. Samavedi, A. R. Whittington and A. S. Goldstein, *Acta Biomater.*, 2013, **9**, 8037–8045.
13 J. C. Arts, N. Verdonschot, B. W. Schreurs and P. Buma, *Biomaterials*, 2006, **27**, 1110–1118.
14 J. R. Venugopal, S. Low, A. T. Choon, A. B. Kumar and S. Ramakrishna, *Artif. Organs*, 2008, **32**, 388–397.
15 T. J. Webster, C. Ergun, R. H. Doremus, R. W. Siegel and R. Bizios, *J. Biomed. Mater. Res.*, 2000, **51**, 475–483.
16 G. Wei and P. X. Ma, *Biomaterials*, 2004, **25**, 4749–4757.
17 A. Bigi, E. Boanini and M. Gazzano, *Biomineralization and Biomaterials*, 2016, pp. 235–266.
18 D. Marx, A. R. Yazdi, M. Papini and M. Towler, *Bone Rep.*, 2020, **12**, 100273.
19 P. J. Marie, *Curr. Opin. Pharmacol.*, 2005, **5**, 633–636.
20 F. Yang, D. Yang, J. Tu, Q. Zheng, L. Cai and L. Wang, *Stem Cells*, 2011, **29**, 981–991.
21 M. S. Rybchyn, M. Slater, A. D. Conigrave and R. S. Mason, *J. Biol. Chem.*, 2011, **286**, 23771–23779.
22 R. G. G. Russell, *Bone*, 2011, **49**, 2–19.
23 A. Cheng, A. Mavrokokki, G. Carter, B. Stein, N. Fazzalari, D. Wilson and A. Goss, *Aust. Dent. J.*, 2005, **50**, S4.
24 R. Russell, N. Watts, F. Ebetino and M. Rogers, *Osteoporosis Int.*, 2008, **19**, 733–759.
25 N. Maruotti, A. Corrado, A. Neve and F. P. Cantatore, *Eur. J. Clin. Pharmacol.*, 2012, **68**, 1013–1018.
26 A. Corrado, A. Neve, N. Maruotti, A. Gaudio, A. Marucci and F. P. Cantatore, *Clin. Exp. Rheumatol.*, 2010, **28**, 873.
27 E. Boanini, P. Torricelli, M. Gazzano, M. Fini and A. Bigi, *Biomaterials*, 2012, **33**, 722–730.
28 E. Boanini, P. Torricelli, M. Gazzano, E. D. Bella, M. Fini and A. Bigi, *Biomaterials*, 2014, **35**, 5619–5626.
29 E. Boanini, P. Torricelli, F. Sima, E. Axente, M. Fini, I. N. Mihailescu and A. Bigi, *J. Colloid Interface Sci.*, 2015, **448**, 1–7.
30 M. G. Raucci, U. D'Amora, A. Ronca and L. Ambrosio, *Adv. Healthcare Mater.*, 2020, **9**, 2000349.
31 Q. Hou, A. Paul and K. M. Shakesheff, *J. Mater. Chem.*, 2004, **14**, 1915–1923.
32 N. E. Fedorovich, M. H. Oudshoorn, D. van Geemen, W. E. Hennink, J. Alblas and W. J. Dhert, *Biomaterials*, 2009, **30**, 344–353.
33 B. Balakrishnan, N. Joshi and R. Banerjee, *J. Mater. Chem. B*, 2013, **1**, 5564–5577.
34 Y. Ou and M. Tian, *J. Mater. Chem. B*, 2021, **9**, 7955–7971.
35 X. Xue, Y. Hu, Y. Deng and J. Su, *Adv. Funct. Mater.*, 2021, **31**, 2009432.
36 R. Jayakumar, M. Prabaharan, S. Nair, S. Tokura, H. Tamura and N. Selvamurugan, *Prog. Mater. Sci.*, 2010, **55**, 675–709.
37 W. Müller, M. Neufurth, S. Wang, E. Tolba, H. Schröder and X. Wang, *Eur. Cell. Mater.*, 2016, **31**, 174–190.
38 S. Sakai, Y. Yamada, T. Zenke and K. Kawakami, *J. Mater. Chem.*, 2009, **19**, 230–235.
39 Y. Lu, L. Li, Y. Zhu, X. Wang, M. Li, Z. Lin, X. Hu, Y. Zhang, Q. Yin and H. Xia, *ACS Appl. Mater. Interfaces*, 2018, **10**, 127–138.
40 B. L. Guo, J. F. Yuan and Q. Y. Gao, *J. Appl. Polym. Sci.*, 2007, **104**, 1279–1284.
41 X. Mo, H. Iwata, S. Matsuda and Y. Ikada, *J. Biomater. Sci., Polym. Ed.*, 2000, **11**, 341–351.
42 J. Maia, L. Ferreira, R. Carvalho, M. A. Ramos and M. H. Gil, *Polymer*, 2005, **46**, 9604–9614.
43 S. R. Van Tomme and W. E. Hennink, *Expert Rev. Med. Devices*, 2007, **4**, 147–164.
44 H. T. Peng and P. N. Shek, *J. Mater. Sci.: Mater. Med.*, 2009, **20**, 1753–1762.
45 C. Yan, T. Yang, S. Zhu and H. Wu, *J. Mater. Chem. B*, 2017, **5**, 3697–3705.
46 Z. Li, B. Li, X. Li, Z. Lin, L. Chen, H. Chen, Y. Jin, T. Zhang, H. Xia and Y. Lu, *Carbohydr. Polym.*, 2021, **267**, 118155.
47 J.-P. Draye, B. Delaey, A. Van de Voorde, A. Van Den Bulcke, B. Bogdanov and E. Schacht, *Biomaterials*, 1998, **19**, 99–107.
48 L. K. Meena, P. Raval, D. Kedaria and R. Vasita, *Bioact. Mater.*, 2018, **3**, 370–384.
49 M. Saleem, S. Rasheed and C. Yougen, *Sci. Technol. Adv. Mater.*, 2020, **21**, 242–266.
50 M. Głąb, S. Kudłacik-Kramarczyk, A. Drabczyk, J. Walter, A. Kordyka, M. Godzierz, R. Bogucki, B. Tyliszczak and A. Sobczak-Kupiec, *Molecules*, 2021, **26**, 4268.
51 Z. Li, B. Yuan, X. Dong, L. Duan, H. Tian, C. He and X. Chen, *RSC Adv.*, 2015, **5**, 94248–94256.
52 V. Kumar and T. Yang, *Int. J. Pharm.*, 1999, **184**, 219–226.
53 J. Maia, R. A. Carvalho, J. F. Coelho, P. N. Simões and M. H. Gil, *Polymer*, 2011, **52**, 258–265.
54 A. Lisman, B. Butruk, I. Wasiak and T. Ciach, *J. Biomater. Appl.*, 2014, **28**, 1386–1396.
55 H. A. Bilgic, B. Kilic, B. D. Kockaya, B. E. Sarac, A. K. Suloglu, O. Kalayci and C. Karaaslan, *Life Sci.*, 2023, **315**, 121358.
56 N. Momtahan, T. Panahi, N. Poornejad, M. G. Stewart, B. R. Vance, J. A. Struk, A. A. Castleton, B. L. Roeder, S. Sukavaneshvar and A. D. Cook, *ASAIO J.*, 2016, **62**, 340–348.
57 J.-K. Zhang, L. Yang, G.-L. Meng, J. Fan, J.-Z. Chen, Q.-Z. He, S. Chen, J.-Z. Fan, Z.-J. Luo and J. Liu, *Eur. J. Pharmacol.*, 2012, **689**, 31–37.
58 K. Liu, J. Zhao, L. Yang, M. Guan, L. Yuan and Y. Geng, *Int. J. Mol. Med.*, 2020, **45**, 1793–1802.
59 M. Balouiri, M. Sadiki and S. K. Ibnsouda, *J. Pharm. Anal.*, 2016, **6**, 71–79.
60 E. Urnukhsaikhan, B.-E. Bold, A. Gunbileg, N. Sukhbaatar and T. Mishig-Ochir, *Sci. Rep.*, 2021, **11**, 21047.
61 B. T. Amaechi, P. A. AbdulAzees, D. O. Alshareif, M. A. Shehata, P. P. d. C. S. Lima, A. Abdollahi, P. S. Kalkhorani and V. Evans, *BDJ Open*, 2019, **5**, 18.
62 E. Boanini, M. Gazzano and A. Bigi, *Acta Biomater.*, 2010, **6**, 1882–1894.
63 Z. Geng, Z. Cui, Z. Li, S. Zhu, Y. Liang, Y. Liu, X. Li, X. He, X. Yu and R. Wang, *Mater. Sci. Eng., C*, 2016, **58**, 467–477.
64 Z. Zhu, Y. Yang, Y. Fan, L. Zhang, S. Tang, Y. Zhu and X. Zhou, *Environ. Technol. Innovation*, 2022, **28**, 102575.
65 S. J. Kalita, A. Bhardwaj and H. A. Bhatt, *Mater. Sci. Eng., C*, 2007, **27**, 441–449.

66 A. El-Ghannam and P. Ducheyne, in *Bioactive ceramics, Comprehensive Biomaterials*, 2011, vol. 1, pp. 157–179.

67 H. El Boujaady, M. Mourabet, A. El Rhilassi, M. Bennani-Ziatni, R. El Hamri and A. Taitai, *J. Mater. Environ. Sci.*, 2016, **7**, 4049–4063.

68 M. Frasnelli, F. Cristofaro, V. M. Sglavo, S. Dirè, E. Callone, R. Ceccato, G. Bruni, A. I. Cornaglia and L. Visai, *Mater. Sci. Eng., C*, 2017, **71**, 653–662.

69 Z. Li, W. Lam, C. Yang, B. Xu, G. Ni, S. Abbah, K. Cheung, K. Luk and W. Lu, *Biomaterials*, 2007, **28**, 1452–1460.

70 Z.-L. Xu, Y. Lei, W.-J. Yin, Y.-X. Chen, Q.-F. Ke, Y.-P. Guo and C.-Q. Zhang, *J. Mater. Chem. B*, 2016, **4**, 7919–7928.

71 F. Scalera, F. Gervaso, K. Sanosh, A. Sannino and A. Licciulli, *Ceram. Int.*, 2013, **39**, 4839–4846.

72 D. K. Khajuria, R. Razdan and D. R. Mahapatra, *Eur. J. Pharm. Sci.*, 2015, **66**, 173–183.

73 L. Li, N. Wang, X. Jin, R. Deng, S. Nie, L. Sun, Q. Wu, Y. Wei and C. Gong, *Biomaterials*, 2014, **35**, 3903–3917.

74 J. Wu, Q. Zhao, C. Liang and T. Xie, *Soft Matter*, 2013, **9**, 11136–11142.

75 V. Mourya, N. N. Inamdar and A. Tiwari, *Adv. Mater. Lett.*, 2010, **1**, 11–33.

76 Z. Aiping, L. Jianhong and Y. Wenhui, *Carbohydr. Polym.*, 2006, **63**, 89–96.

77 A. Nada, M. El-Sakhawy, S. Kamel, M. Eid and A. M. Adel, *Carbohydr. Polym.*, 2006, **63**, 113–121.

78 B. Ren, X. Chen, S. Du, Y. Ma, H. Chen, G. Yuan, J. Li, D. Xiong, H. Tan and Z. Ling, *Int. J. Biol. Macromol.*, 2018, **118**, 1257–1266.

79 K. Enoch and A. A. Somasundaram, *Int. J. Biol. Macromol.*, 2023, **253**, 127481.

80 Y.-J. Seong, G. Lin, B. J. Kim, H.-E. Kim, S. Kim and S.-H. Jeong, *ACS Omega*, 2019, **4**, 13834–13844.

81 B. Abderrahim, E. Abderrahman, A. Mohamed, T. Fatima, T. Abdesselam and O. Krim, *World J. Environ. Eng.*, 2015, **3**, 95–110.

82 S. Borhan, S. Hesaraki, A.-A. Behnamghader and E. Ghasemi, *J. Mater. Sci.: Mater. Med.*, 2016, **27**, 1–15.

83 X. Ding, X. Li, C. Li, M. Qi, Z. Zhang, X. Sun, L. Wang and Y. Zhou, *ACS Biomater. Sci. Eng.*, 2019, **5**, 4574–4586.

84 Z. Li, C. He, B. Yuan, X. Dong and X. Chen, *Macromol. Biosci.*, 2017, **17**, 1600347.

85 J. Li, X. Liu, S. Park, A. L. Miller, A. Terzic and L. Lu, *J. Biomed. Mater. Res., Part A*, 2019, **107**, 631–642.

86 P. Ding, Y. Lu, C. Zhao, W. Guo and L. Nie, *Mater. Today Commun.*, 2024, **41**, 110463.

87 I. R. Lima, S. R. Santos, D. Santiago, A. M. Rossi and J. M. Granjeiro, *Key Eng. Mater.*, 2008, **361**, 1135–1138.

88 W. Xue, J. L. Moore, H. L. Hosick, S. Bose, A. Bandyopadhyay, W. Lu, K. M. Cheung and K. D. Luk, *J. Biomed. Mater. Res., Part A*, 2006, **79**, 804–814.

89 C. Capuccini, P. Torricelli, F. Sima, E. Boanini, C. Ristoscu, B. Bracci, G. Socol, M. Fini, I. Mihailescu and A. Bigi, *Acta Biomater.*, 2008, **4**, 1885–1893.

90 Y. Cai, T. Gao, S. Fu and P. Sun, *Exp. Ther. Med.*, 2018, **16**, 704–710.

91 W.-C. Lin, C.-C. Lien, H.-J. Yeh, C.-M. Yu and S.-h. Hsu, *Carbohydr. Polym.*, 2013, **94**, 603–611.

92 R. T. Monteiro, F. K. Andrade, N. F. Vasconcelos, K. A. B. Nogueira, R. Petrilli and R. S. Vieira, *Biointerphases*, 2020, **15**(4), 041002.

93 M. Parekh, V. Romano, K. Hassanin, V. Testa, R. Wongvisavavit, S. Ferrari, A. Haneef, C. Willoughby, D. Ponzin and V. Jhanji, *J. Tissue Eng.*, 2021, **12**, 2041731421990536.

94 A. Riemann, B. Schneider, A. Ihling, M. Nowak, C. Sauvant, O. Thews and M. Gekle, *PLoS One*, 2011, **6**, e22445.

95 G.-X. Ni, Z.-P. Yao, G.-T. Huang, W.-G. Liu and W. W. Lu, *J. Mater. Sci.: Mater. Med.*, 2011, **22**, 961–967.

96 E. Boanini, P. Torricelli, M. Fini and A. Bigi, *J. Mater. Sci.: Mater. Med.*, 2011, **22**, 2079–2088.

97 Y. H. Kim, D. S. Yoon, H. O. Kim and J. W. Lee, *Stem Cell. Dev.*, 2012, **21**, 2958–2968.

98 K. Wong, C. Wong, W. Liu, H. Pan, M. Fong, W. Lam, W. Cheung, W. Tang, K. Chiu and K. Luk, *Biomaterials*, 2009, **30**, 3810–3817.

99 B. Pan, A. N. Farrugia, L. B. To, D. M. Findlay, J. Green, K. Lynch and A. C. Zannettino, *J. Bone Miner. Res.*, 2004, **19**, 147–154.

100 S. J. Suratwala, S. K. Cho, J. J. van Raalte, S. H. Park, S. W. Seo, S.-S. Chang, T. R. Gardner and F. Y.-I. Lee, *J. Bone Jt. Surg.*, 2008, **90**, 2189–2196.

101 I. R. Orriss, M. L. Key, K. W. Colston and T. R. Arnett, *J. Cell. Biochem.*, 2009, **106**, 109–118.

102 A. Naidu, P. C. Dechow, R. Spears, J. M. Wright, H. P. Kessler and L. A. Opperman, *Oral Surg. Oral Med. Oral Pathol. Oral Radiol. Endod.*, 2008, **106**, 5–13.

103 X. Zhao, H. Wu, B. Guo, R. Dong, Y. Qiu and P. X. Ma, *Biomaterials*, 2017, **122**, 34–47.

104 K. Yang, X. Zhou, Z. Li, Z. Wang, Y. Luo, L. Deng and D. He, *ACS Appl. Mater. Interfaces*, 2022, **14**, 43010–43025.

105 N. Sudarshan, D. Hoover and D. Knorr, *Food Biotechnol.*, 1992, **6**, 257–272.

106 X. F. Liu, Y. L. Guan, D. Z. Yang, Z. Li and K. D. Yao, *J. Appl. Polym. Sci.*, 2001, **79**, 1324–1335.

107 A. Anitha, V. D. Rani, R. Krishna, V. Sreeja, N. Selvamurugan, S. Nair, H. Tamura and R. Jayakumar, *Carbohydr. Polym.*, 2009, **78**, 672–677.

108 C. Simons, S. E. Walsh, J. Y. Maillard and A. Russell, *Lett. Appl. Microbiol.*, 2000, **31**, 299–302.

109 M. A. Aziz, J. D. Cabral, H. J. Brooks, S. C. Moratti and L. R. Hanton, *Antimicrob. Agents Chemother.*, 2012, **56**, 280–287.

110 N. Baheiraei, H. Eyni, B. Bakhshi, R. Najafloo and N. Rabiee, *Sci. Rep.*, 2021, **11**, 8745.

111 J. Liu, S. C. Rawlinson, R. G. Hill and F. Fortune, *Dent. Mater.*, 2016, **32**, 412–422.

112 A. Leon, L. Liu, Y. Yang, M. P. Hudock, P. Hall, F. Yin, D. Studer, K.-J. Puan, C. T. Morita and E. Oldfield, *J. Med. Chem.*, 2006, **49**, 7331–7341.

113 Y. Lu, M. Li, L. Li, S. Wei, X. Hu, X. Wang, G. Shan, Y. Zhang, H. Xia and Q. Yin, *Mater. Sci. Eng., C*, 2018, **82**, 225–233.